Resolving Material-Specific Structures within Fe₃O₄|γ-Mn₂O₃ Core|Shell Nanoparticles Using Anomalous Small-Angle X-ray Scattering

Kathryn L. Krycka,[†,*] Julie A. Borchers,[†] German Salazar-Alvarez,[‡] Alberto López-Ortega,[§,⊥] Marta Estrader,[‡,§,⊥] Sònia Estradé,[∥,¶] Elin Winkler,[#] Roberto Daniel Zysler,[#] Jordi Sort,[⊥,▲] Francesca Peiró,[¶] Maria Dolors Baró,[⊥] Chi-Chang Kao,[▼] and Josep Nogués[§,⊥,▲]

[†]NIST Center for Neutron Research, National Institute of Standards and Technology, Gaithersburg, Maryland 20899, United States, [‡]Department of Materials and Environmental Chemistry, Stockholm University, S-10691 Stockholm, Sweden, [§]CIN2(ICN-CSIC) and Universitat Autònoma de Barcelona, Catalan Institute of Nanotechnology (ICN), Campus de la UAB, E-08193 Bellaterra (Barcelona), Spain, [⊥]Departament de Física, Universitat Autònoma de Barcelona, E-08193 Bellaterra (Barcelona), Spain, [∥]TEM-MAT, CCiT, Universitat de Barcelona, Solè i Sabarí s 1, E-08028 Barcelona, Spain, [¶]LENS, MIND-IN2UB, Departament d'Electrònica, Universitat de Barcelona, Martí i Franquès 1, E-08028 Barcelona, Spain, [#]Centro Atómico Bariloche, CNEA-CONICET, 8400 S.C. de Bariloche, Río Negro, Argentina, [▲]Institució Catalana de Recerca i Estudis Avançats (ICREA), 08010 Barcelona, Spain, and [▼]Stanford Synchrotron Radiation Lightsource, Menlo Park, California 94025, United States

ABSTRACT Here it is demonstrated that multiple-energy, anomalous small-angle X-ray scattering (ASAXS) provides significant enhancement in sensitivity to internal material boundaries of layered nanoparticles compared with the traditional modeling of a single scattering energy, even for cases in which high scattering contrast naturally exists. Specifically, the material-specific structure of monodispersed Fe₃O₄|γ-Mn₂O₃ core|shell nanoparticles is determined, and the contribution of each component to the total scattering profile is identified with unprecedented clarity. We show that Fe₃O₄|γ-Mn₂O₃ core|shell nanoparticles with a diameter of 8.2 ± 0.2 nm consist of a core with a composition near Fe₃O₄

surrounded by a $(Mn_xFe_{1-x})_3O_4$ shell with a graded composition, ranging from $x \approx 0.40$ at the inner shell toward $x \approx 0.46$ at the surface. Evaluation of the scattering contribution arising from the interference between material-specific layers additionally reveals the presence of Fe₃O₄ cores without a coating shell. Finally, it is found that the material-specific scattering profile shapes and chemical compositions extracted by this method are independent of the original input chemical compositions used in the analysis, revealing multiple-energy ASAXS as a powerful tool for determining internal nanostructured morphology even if the exact composition of the individual layers is not known *a priori*.
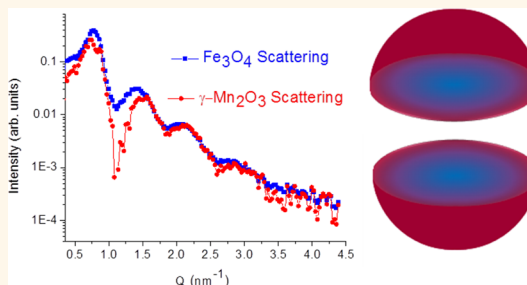
KEYWORDS: core|shell nanoparticles · Fe₃O₄ · γ-Mn₂O₃ · neutron scattering · anomalous X-ray scattering · SAXS

The exceptional impact of nanoparticles in industry and research during the past decade is undeniable, spreading in fields with everyday applications such as cosmetics to high-end biotechnology.[1−5] Interestingly, advances in synthetic chemistry have allowed reaching beyond conventional nanoparticles into more complex hybrid structures comprising two (or more) materials such as core|shell particles.[6−8] These systems can combine in a synergetic way the diverse properties (*e.g.*, catalytical, optical, magnetic, or biomedical) of the different constituents leading to multifunctional materials with novel and improved characteristics, paving the way for an even broader applicability of nanoparticles. Given the unprecedented ability to control growth parameters during the synthesis (*i.e.*, core diameter, shell thickness, and material composition), the overall properties of the particles can be accurately tailored to match specific applications. In fact, core|shell nanoparticles have an extra degree of freedom since the properties can often be tuned not only by the core and shell characteristics but also through their interactions.[9−18] Typically, the properties of core| shell nanoparticles depend critically on the
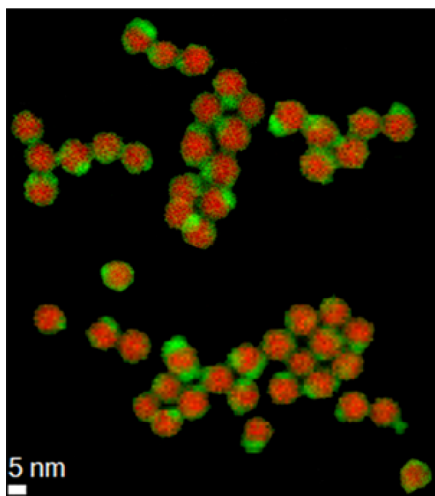
Figure 1. STEM with EELS Fe (red) and Mn (green) elemental mapping for $Fe_3O_4|\gamma$-Mn_2O_3 core|shell nanoparticles.

structural morphology such as the thickness (and variability) of the constituent layers, their composition, and the sharpness of interfaces. Consequently, the precise determination of these parameters is vital to understanding and fine-tuning the functionalities of the core|shell systems.

While many techniques exist for non-location-specific chemical analysis, such as Mössbauer spectroscopy[19,20] and X-ray absorption spectroscopy (XAS), characterizing the internal structure of such core|shell nanoparticles continues to be a challenging endeavor. Even scanning transmission electron microscopy (STEM) imaging with electron energy loss spectroscopy (EELS) analysis,[21−27] which can often give an accurate account of the morphology of the particles (as shown in Figure 1 applied to a subset of our 8.2 nm $Fe_3O_4|\gamma$-Mn_2O_3 core|shell nanoparticles), remains insufficient since only a small number of particles can be analyzed. For this reason, complementary techniques such as neutron and X-ray diffractive methods are desirable since they measure macroscopic amounts of sample (*i.e.*, millions of nanoparticles), giving a better picture of the overall morphology and dispersion. Yet, small-angle X-ray scattering (SAXS), which is very useful in evaluating particle size and polydispersity for homogeneous nanoparticles,[28,29] suffers from an inability to definitively pinpoint chemical boundaries within core|shell nanoparticles, even in cases for which high material contrast exists. To this end, the multiple-energy, anomalous SAXS (ASAXS) approach[30−33] offers renewed potential for the analysis of core|shell nanoparticles.[34,35] Here we demonstrate the full utility of the ASAXS technique to unambiguously elucidate the fine structural details for a tightly packed powder of 8.2 ± 0.2 nm diameter core| shell nanoparticles nominally composed of Fe_3O_4 cores and γ-Mn_2O_3 shells.[36] The resonant X-ray results indicate not only the presence of a clear

core|shell structure but also the existence of an intermediate shell of mixed composition, in agreement with TEM and EELS analysis. Moreover, the study directly reveals differences in the degree of coating, which are largely undetectable by any other techniques.

SAXS and small-angle neutron scattering, SANS, provide structural information on the micrometer to subnanometer length scale (Figure 2a). The measured intensity, *I*, which is plotted as a function of scattering wavevector, *Q*, in Figure 2b for SANS and Figure 2c for SAXS, is proportional to the material-specific scattering length density squared, $|\rho|^2$. For all variables, ' and '' denote the real (scattering) and imaginary (absorbing) components. Information regarding the spatial distribution of the *J* scattering centers, located at the relative positions, R_J, is contained within the Fourier transform, $\mathscr{F}$ as

$$
I(Q) \propto \left| \sum_{J \text{ scatterers}} (\rho'_J + i\rho''_J)e^{i\vec{Q}\cdot\vec{R}_J} \right|^2
$$

$$
= \left| \sum_{K \text{ materials}} \rho_K \mathscr{F}_K \right|^2 \quad (1)
$$

From a modeling standpoint, $|\mathscr{F}|^2$ is viewed as the convolution of the structure factor (nanoparticle packing), $|S|^2$, with the form factor (internal nanoparticle structure), $|F|^2$.

Although diffraction methods can be extremely sensitive to external nanoparticle diameter, they are relatively insensitive to internal structures. As the room temperature SANS data underscore (see Figure 2b and Supporting Information), even a high ρ contrast ratio >4 (refer to Table 1) is not sufficient to distinguish through modeling[37] whether the nanoparticles' $|F|^2$ is closer to homogeneous Fe−Mn oxide spheres or arises from distinctive $Fe_3O_4|\gamma$-Mn_2O_3 core|shell nanoparticles.

Importantly, material sensitivity (and, thus, sensitivity to internal layering) may be enhanced by collecting multiple, energy-dependent scattering patterns of varied ρ values. For neutrons, this can be achieved in many organic systems through hydrogen−deuterium substitution,[38,39] while for X-rays, ρ changes dramatically as a function of energy about atomic absorption edges, coined anomalous or resonant scattering.[40] Thus, as shown in Figure 2c, anomalous scattering patterns were acquired at the Mn and Fe K-edges,[41] 6535 and 7112 eV, respectively, and off-resonance at 6000 eV (Table 1). Yet, aside from changes in total intensity and a slight low-Q oscillation shift, the profiles appear to be strikingly similar. The reason for this is that the scattering is heavily influenced by scattering interference between the Fe and Mn oxides (also referred to as a cross-term, which will be explicitly evaluated later).

To illustrate this, consider a two-layer system labeled as α and β ($\alpha = Fe_3O_4$ and $\beta = \gamma\text{-}Mn_2O_3$)

$$I(Q) \propto \underbrace{|\rho_\alpha|^2|\mathfrak{F}_\alpha|^2}_{I_\alpha} + \underbrace{|\rho_\beta|^2|\mathfrak{F}_\beta|^2}_{I_\beta} +$$
$$\underbrace{2(\rho_\alpha'\rho_\beta' + \rho_\alpha''\rho_\beta'')\overbrace{(\mathfrak{F}_\alpha'\mathfrak{F}_\beta' + \mathfrak{F}_\alpha''\mathfrak{F}_\beta'')}^{\mathfrak{F}_{Int1}}}_{I_{Int1}} + \underbrace{2(\rho_\alpha'\rho_\beta'' - \rho_\alpha''\rho_\beta')\overbrace{(\mathfrak{F}_\alpha''\mathfrak{F}_\beta' - \mathfrak{F}_\alpha'\mathfrak{F}_\beta'')}^{\mathfrak{F}_{Int2}}}_{I_{Int2}},$$
$$(2)$$

where cross-terms, I_{Int1} and I_{Int2}, each depend on both ρ_α and ρ_β. It is clear that material-specific scattering cannot simply be extracted from the subtraction of scattering profiles obtained at energies just below and on a relevant absorption edge, as is commonly assumed.

However, the *simultaneous analysis* of multiple-energy ASAXS profiles[34,35] does provide the means to uniquely separate material-specific $|\mathcal{F}|^2$ values. The number of input scattering scans with different energies must be equivalent to the total number of material-specific scattering terms and interference terms of interest. First, we note that I_{Int2} of eq 2 is negligibly small (Table 1) and can be disregarded. Thus, the remaining scattering terms can be uniquely isolated using only three scattering inputs taken at three different energies, E_1–E_3 (Figure 2c). At each point in Q-space, the material-specific scattering contributions are determined by inverting the matrix in eq 3.

Application of eq 3 to the data of Figure 2c results in the separation of Fe_3O_4 and $\gamma\text{-}Mn_2O_3$ material-specific scattering ($|\mathcal{F}_\alpha|^2$ and $|\mathcal{F}_\beta|^2$) plus the $\gamma\text{-}Mn_2O_3$–Fe_3O_4 cross-term ($\mathcal{F}_{Int1}$), as plotted in Figure 3a. It is worth noting that this separation approach yields scattering profiles that are directly correlated to the number of chemical formula units per volume squared rather than the traditional scattering length density squared which varies as a function of incident X-ray energy. Considering that the cross-term contributes twice as much as $|\mathcal{F}_\alpha|^2$ or $|\mathcal{F}_\beta|^2$ (eq 2) to the overall scattering intensity, this explains the similarity in scattering shape at all energies, as shown in Figure 2c. Although the interference term can be positively or negatively valued, simulation suggests that for core|shell morphology the cross-term will contribute negatively over the first oscillation, as experimentally observed. Moreover, the existence of a non-zero cross-term implies that there must be a correlation between the Fe_3O_4 and $\gamma\text{-}Mn_2O_3$ layers; that is, a significant proportion of them must coexist within the same nanoparticles with a repeating morphology particle-to-particle.

The difference in the material-specific scattering profiles is especially striking at 1.1 nm^{-1} where the $\gamma\text{-}Mn_2O_3$ scattering contains a noticeably sharper dip than the Fe_3O_4 scattering (Figure 3b). Above $Q = 1.5$ nm^{-1}, the profiles look similar. Extensive simulation suggests that if the relative intensity of each energy-dependent experimental profile is not preserved to within a few percent, then the extracted material-specific profiles will typically assume a common scattering shape similar to that of the composite nanoparticle. Thus, the low-intensity region of $Q \geq 1.5$ nm^{-1} is especially susceptible to any background subtraction issues during the material-specific scattering reconstruction. Even so, there are periodic differences, indicated by green arrows (Figure 3b). Division of the extracted Fe_3O_4 profile by the $\gamma\text{-}Mn_2O_3$ profile, $|\mathcal{F}|_{Fe_3O_4}/|\mathcal{F}|_{\gamma-Mn_2O_3}$, further highlights these periodic differences (Figure 3c). These differences indicate that the Fe_3O_4 and $\gamma\text{-}Mn_2O_3$ components must be present in different morphological distributions as a function of radius within the nanoparticles, which for spherical nanoparticles would correspond to a radially graded (*i.e.*, core|shell or core|shell|shell) structure.

RESULTS AND DISCUSSION

Modeling of the material-specific X-ray scattering provides ensemble-averaged information regarding nanoparticle core and shell dimensions, compositional uniformity, size polydispersity, nanoparticle packing, and the relative ratio of Mn to Fe present. As discussed previously in regard to modeling of the SANS data, $|\mathcal{F}|^2 = |F|^2|S|^2$, where $|F|^2$ and $|S|^2$ are the form and structure factors, respectively.

Outermost Diameter. The $\gamma\text{-}Mn_2O_3$ (Figure 3a,b) distribution extends out to the edge of the nanoparticle with scattering that is consistent with a spherical model of exterior diameter 8.2 ± 0.1 nm. The corresponding interior can vary from a sphere of uniform density to a sphere centrally devoid of Mn up to the first 1.8 nm in diameter. (Even element-specific diffraction is most sensitive to the outermost dimensions of that layer since more material resides there.) In contrast, the Fe_3O_4 oscillations and slope (Figure 3a,b) cannot be fit by a sphere of uniform density. Instead, a graded model where the amount of Fe_3O_4 decreases radially toward the surface is required. Depending on the steepness of gradient chosen, the outer diameter can range from 8.2 nm (less gradient) to 8.4 nm (more gradient). However, since we know that the Fe_3O_4 should be concentrated toward the interior of the core|shell particles based on knowledge about their

$$\underbrace{\begin{bmatrix} |\rho_\alpha(E_1)|^2 & |\rho_\beta(E_1)|^2 & 2(\rho_\alpha'(E_1)\rho_\beta'(E_1) + \rho_\alpha''(E_1)\rho_\beta''(E_1)) \\ |\rho_\alpha(E_2)|^2 & |\rho_\beta(E_2)|^2 & 2(\rho_\alpha'(E_2)\rho_\beta'(E_2) + \rho_\alpha''(E_2)\rho_\beta''(E_2)) \\ |\rho_\alpha(E_3)|^2 & |\rho_\beta(E_3)|^2 & 2(\rho_\alpha'(E_3)\rho_\beta'(E_3) + \rho_\alpha''(E_3)\rho_\beta''(E_3)) \end{bmatrix}}_{Known\ Coefficients} \underbrace{\begin{bmatrix} |\mathfrak{F}_\alpha|^2 \\ |\mathfrak{F}_\beta|^2 \\ \mathfrak{F}_{Int1} \end{bmatrix}}_{Variables\ To\ Solve} \propto \underbrace{\begin{bmatrix} I(E_1) \\ I(E_2) \\ I(E_3) \end{bmatrix}}_{Numerical\ Inputs} \quad (3)$$
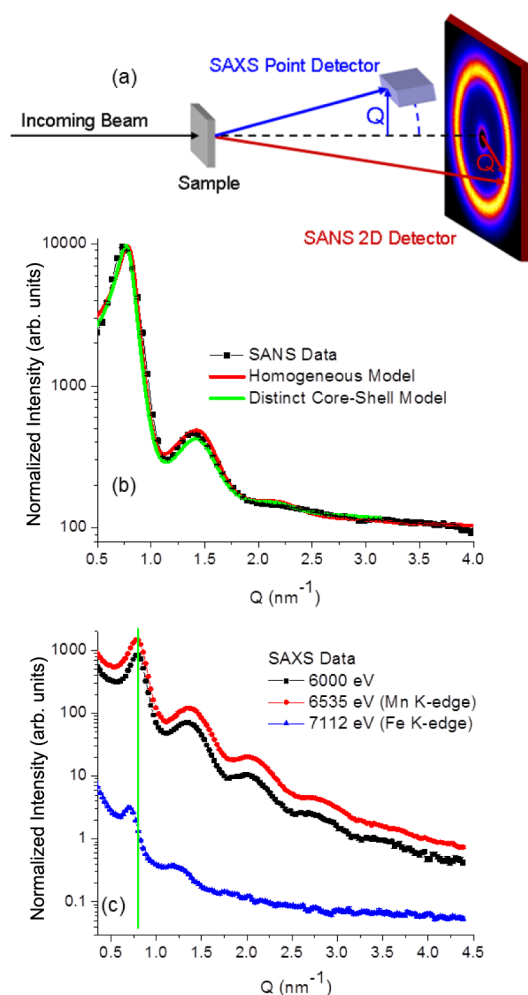
Figure 2. (a) Schematic of SAXS and SANS setups (not drawn to scale). Note that the experiments are carried out separately in different user facilities. (b) SANS data fitted using models based on homogeneous Fe−Mn oxide nanoparticles (red curve) or distinct Fe_3O_4 core and γ-Mn_2O_3 shell structure (green curve). (c) SAXS data taken away from resonance (6000 eV) and on the Mn and Fe K-edges (6535 and 7112 eV, respectively). The vertical green line emphasizes low-Q oscillation shift observed at the Fe K-edge. The statistical counting error bars for SANS and SAXS data are included but are too small to be seen.

TABLE 1. Scattering Length Densities ($\rho = \rho' + i\rho''$, in 10^{-4} nm^{-2}) for Various Crystallographic Phases at Different Energies[a]

|	pPhase	6000 eV[b]	6535 eV[b]	7112 eV[b]	$\lambda_n = 0.5$ nm[c]
ρ'	γ-Fe_2O_3	40.62	39.95	29.90	7.17
	Fe_3O_4	40.00	39.32	29.05	6.95
	γ-Mn_2O_3	33.74	25.03	34.30	1.71
	Mn_3O_4	48.65	35.59	49.50	1.54
ρ''	γ-Fe_2O_3	0.8259	0.7083	4.561	
	Fe_3O_4	0.8328	0.7144	2.536	
	γ-Mn_2O_3	0.6279	2.184	3.380	
	Mn_3O_4	0.9267	3.263	5.059	

[a] From ref 41. Scattering length densities were calculated using mass densities of 4.90, 5.18, 4.50, and 4.86 g/cm^3 for γ-Fe_2O_3, Fe_3O_4, γ-Mn_2O_3, and Mn_3O_4, respectively. [b] X-ray. [c] Neutrons.

chemical synthesis,[36] we impose the constraint that the Fe_3O_4 outer diameter should not exceed that of the γ-Mn_2O_3. This constrains the average particle diameter to be 8.2 ± 0.2 nm.

Bimodal Distribution. The sharp γ-Mn_2O_3 dip at $Q = 1.1$ nm^{-1} (Figure 4a) is indicative of very low polydispersity,[37] on the order of 2%. In light of the monodispersity of the γ-Mn_2O_3 shells, the associated Fe_3O_4 portion of the core|shell particles should also be monodisperse, yet the observed scattering (Figure 4b) does not display such sharp features. To reconcile this, a bimodal model comprising two different types of nanoparticles containing Fe_3O_4 is necessary. The model consists of (i) monodisperse Fe_3O_4 core with reduced Fe density shell nanoparticles (whose outer shell diameter primarily dictates the dip locations observed) which are correlated with the γ-Mn_2O_3 shells, and (ii) uncoated seeds (whose contributions smooth out the dips) which are uncorrelated with the γ-Mn_2O_3 shells. This simple model can explain the diffusive Fe_3O_4 features without resorting to an unphysically large polydispersity for the Fe_3O_4 distribution. The reciprocal space (Q) region surveyed was optimized for larger particles, and thus, it does not cover a full oscillatory pattern of the seeds necessary for a rigorous determination of their sizes. The modeled seed diameters ranged from $\approx$2.2 to 3.4 nm. The best Fe-based structure factor fit encompassing both the Fe_3O_4 component of the core|shell nanoparticles and of the Fe_3O_4 uncoated seeds consists of a hard-sphere radius[37] of 4.2 nm and volume fraction of 0.44. The γ-Mn_2O_3 hard-sphere structure factor diverges slightly from this with a volume fraction of 0.50 and hard-sphere radius of 4.0 nm required to capture the higher Q shift of the first peak (Figure 3a,b).

Layer Densities. Given these experimental constraints, the representative model (Figure 4a,b insets) consists of a core|shell|shell nanoparticle of variable density. The inner core radius is set at 0.4 ± 0.1 nm (to accommodate polydispersity), the inner shell thickness is 2 nm, and the remaining outer shell thickness is 1.7 nm (adding up to a total diameter of 8.2 ± 0.2 nm). Since we do not observe large changes in the relative densities of Fe_3O_4 and γ-Mn_2O_3 between the inner and outer shells, we feel this level of shell delineation provides sufficient grading without over determining the system. However, it should be noted that the choice of interior shell radii is somewhat arbitrary and other shell radii choices yield similar results. Within this model, the Fe_3O_4 density (number of formula units per volume multiplied by a scalar) is best fit from the interior to exterior regions with values of 5.31, 2.65, and 2.32 units/volume, respectively (Figure 4b). The γ-Mn_2O_3 component of our core|shell|shell model returns densities (also in formula units per volume that are consistently scaled with and directly comparable to the Fe_3O_4 densities) of 0, 2.70, and 3.00 units/volume
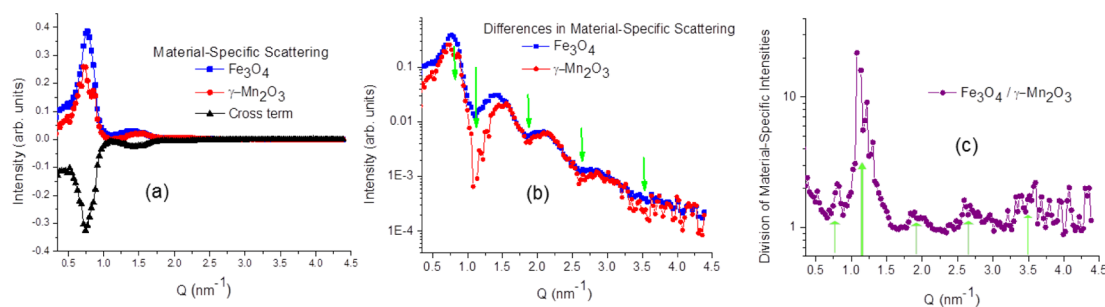
Figure 3. (a) Extracted, material-specific scattering profiles and cross-term. (b) Arrows pinpoint the periodic differences between Fe_3O_4 and γ-Mn_2O_3. (c) Division of the material-specific profiles, $|\mathscr{F}_{Fe_3O_4}|^2/|\mathscr{F}_{\gamma-Mn_2O_3}|^2$, highlight the variation between Fe_3O_4 and γ-Mn_2O_3 scattering and indicate a difference in their nanoparticle morphologies.
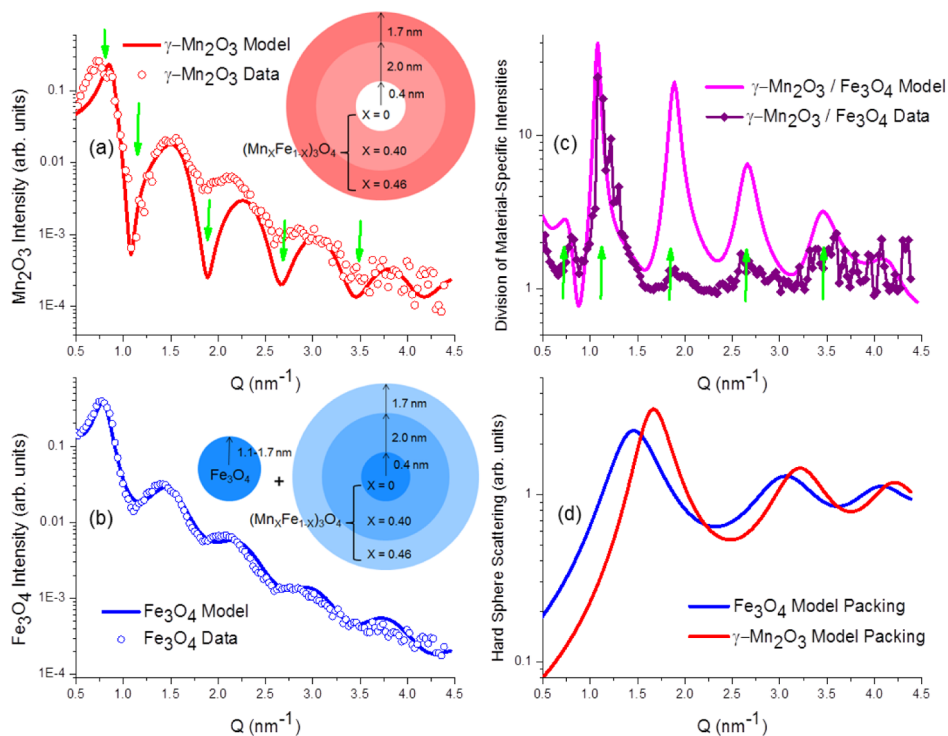

Figure 4. (a) γ-Mn_2O_3 scattering profile and fit where dips highlighted with arrows correspond to those of Figure 3a. (b) Fe_3O_4 scattering profile and fit. Although the insets in (a) and (b) which depict the γ-Mn_2O_3 and Fe_3O_4 portions of the model are not drawn to scale, their fit dimensions are listed exactly as modeled. (c) Division of Fe_3O_4 and γ-Mn_2O_3 modeled scattering profiles reproduces the experimental features of Figure 3c. (d) Hard-sphere model $|S|^2$ values of core|shell nanoparticles and uncoated seed nanoparticles.

from interior to exterior, respectively (Figure 4a). The γ-Mn_2O_3 fit is fairly insensitive to the core region. Yet, it is reasonable to expect that the combined γ-Mn_2O_3 plus Fe_3O_4 density should not vary significantly throughout the particle and, thus, the sum should be close to 5.3 units/volume for all layers. The Fe_3O_4 core region fit value of 5.31 units/volume hence drives the resulting γ-Mn_2O_3 density toward zero, though we cannot completely exclude the possibility that some Mn might reside within the core region. It is worthwhile to note that the division of the γ-Mn_2O_3 and Fe_3O_4 models (Figure 4c) reproduces all of the primary experimental features observed in Figure 3c and strongly reinforces the core|graded shell model.

Seed Fraction Estimate. As modeled, the uncoated Fe_3O_4 seeds can vary between 2.2 and 3.4 nm in diameter. When these seeds are modeled with pure Fe_3O_4 spheres with a diameter of 2.2 nm and a polydispersity of 30% (Figure 4b), their scattering profile must be scaled by a factor of 0.15 compared with the core|shell particles, indicating that the number of uncoated seeds are $\approx$15% that of the core|shell particles. This sets an upper limit for the amount of uncoated seeds. If we employ a larger seed model closer to 3.4 nm in diameter, this seed/core|shell ratio drops as the seed volume squared (*i.e.*, $\approx$4%).

Structure Factor Variation. The difference in modeled packing structure $|S|^2$ for the γ-Mn_2O_3 and Fe_3O_4
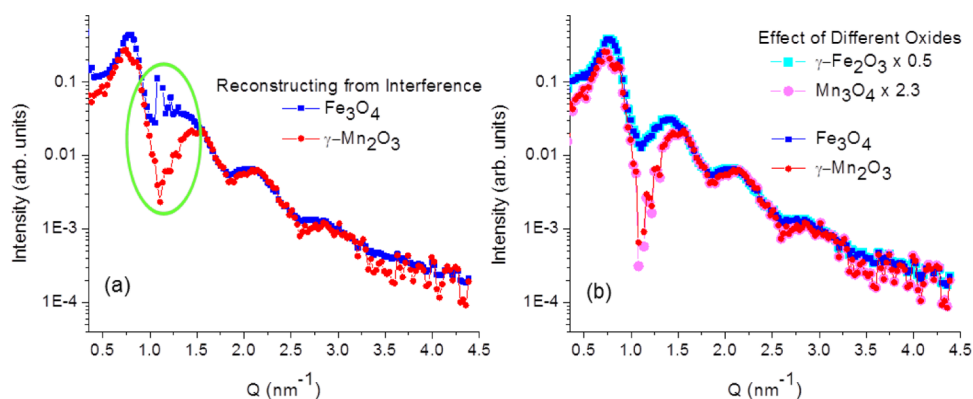
Figure 5. (a) Material-specific scattering reconstruction obtained using eq 4. (b) Effect of oxide variation in material-specific profile reconstruction using eq 3.

scattering contributions, depicted in Figure 4d, can arise only if a portion of the Mn and Fe atoms are not all contained within the same set of nanoparticles, consistent with Fe_3O_4-only seeds. (Note that this is by no means inconsistent with the presence of a cross-term, Figure 3a, which arises from Mn and Fe atoms contained within the set of nanoparticles and which can be attributed to the core−shell nanoparticles.) The shift to slightly larger average spacing between particles and a slightly lower packing density (embodied by $|S|^2$ of the Fe_3O_4 compared with γ-Mn_2O_3, Figure 4d) is also consistent with the presence of randomly dispersed, uncoated Fe_3O_4 seeds. Moreover, the experimentally observed shift of the lowest Q peak in the raw ASAXS scattering (Figure 2c) to a lower Q value at the Fe K-edge would be unexplained in the absence of a bimodal distribution. Although it may seem counter-intuitive that the peak should shift toward lower Q with decreased Fe scattering contribution at 7112 eV when the Fe_3O_4 $|S|^2$ peaks at lower Q than the γ-Mn_2O_3 $|S|^2$ (Figure 4d), we note that the large, negatively valued cross-term (whose peak placement is determined by both the γ-Mn_2O_3 and the Fe_3O_4) also diminishes at the Fe K-edge.

Cross-Term. As a self-consistency check, we note that the third solved term from eq 3, $\mathscr{F}_{Int1}$ (*i.e.*, the cross-term), contains additional information about the material-specific $|S|^2$ values. Division of the extracted terms, $|\mathscr{F}_{Int1}|^2$ and $|\mathscr{F}_{\alpha,\beta}|^2$, yields

$$\mathscr{F}_{Int1}/(|\mathscr{F}_{\alpha,\beta}|^2) = |F_{\beta,\alpha}|^2(S_\alpha'^2 S_\beta'^2 + S_\alpha''^2 S_\beta''^2 + 2S_\alpha' S_\beta' S_\alpha'' S_\beta'')/|S_{\alpha,\beta}|^2 \quad (4)$$

where F for a spherically symmetric object is always real. If $S_\alpha = S_\beta$ ($S_{Fe_3O_4} = S_{\gamma\text{-}Mn_2O_3}$), we should be able to re-extract $|\ddot{\mathscr{F}}_{Fe_3O_4}|^2$ and $|\ddot{\mathscr{F}}_{\gamma-Mn_2O_3}|^2$ using

$$\mathscr{F}_{Int1}/(|\mathscr{F}_{\alpha,\beta}|^2) = |S_{\beta,\alpha}|^2 |F_{\beta,\alpha}|^2 = |\ddot{\mathscr{F}}_{\beta,\alpha}|^2 \quad (5)$$

where the double dot in $|\ddot{\mathscr{F}}_{\alpha,\beta}|$ indicates that the previously extracted $\mathscr{F}_{Int1}$ and $|\mathscr{F}_{\alpha,\beta}|^2$ (eqs 2 and 3) were utilized in this second-order reconstruction. The result of this procedure is shown in Figure 5a. Although

features similar to Figure 3b are reproduced, the reconstruction using eq 4 differs noticeably in the circled region (specifically where the derived $|S_{Fe_3O_4}|^2$ and $|S_{\gamma\text{-}Mn_2O_3}|^2$ most strongly diverge in Figure 4d). This deviation confirms that $S_{Fe_3O_4}$ and $S_{\gamma\text{-}Mn_2O_3}$, though similar, are not identical. The result is again in full agreement with our differing $|S|^2$ fits (Figure 4d) and the experimental, first oscillation shift to lower Q at the Fe K-edge (Figure 2c), and it reinforces the model consisting of core|graded shell nanoparticles residing alongside uncoated Fe_3O_4 seeds.

Mn to Fe Ratio. The combined γ-Mn_2O_3 and Fe_3O_4 core|graded shell fits produce a composite nanoparticle tending toward Fe_3O_4 in the center surrounded by a graded shell composed of both Fe and Mn oxide (Figure 4). Using the fits described above, the net chemical compositions are 5.31 Fe_3O_4/volume|2.65 Fe_3O_4/volume + 2.70 γ-Mn_2O_3/volume|2.32 Fe_3O_4/volume + 3.00 γ-Mn_2O_3/volume. If we were to assume that the shells are homogeneously mixed, then we can rewrite the compositions in terms of Mn-ferrite as $(Mn_xFe_{1-x})_3O_{4.2}$, where x ranges from 0.40 to 0.46 for the average inner and outer shell regions, respectively. Since the ASAXS technique is optimized to be highly sensitive to the Fe and Mn content, yet less sensitive to the oxygen content, it is likely that the oxygen stoichiometric number is in fact closer to 4.0.

Chemical Sensitivity. To determine the sensitivity of this technique to oxide type, we substitute the ρ values (Table 1) of γ-Fe_2O_3 and Mn_3O_4 for Fe_3O_4 and γ-Mn_2O_3, respectively, into eq 3. As shown in Figure 5b, the basic scattering shapes remain unaltered, while the difference between Fe and Mn oxide scattering profiles changes by a relative factor of 4.6. Taking into account the scaling of Fe oxide core|shell and Mn oxide shell scattering contributions with the fact that the measured intensity is proportional to density *squared*, we extract a mixed-shell composition of 7.50 γ-Fe_2O_3/volume|3.57 γ-Fe_2O_3/volume + 1.78 Mn_3O_4/volume|3.18 γ-Fe_2O_3/volume + 1.98 Mn_3O_4/volume. Recast in terms of a composite ferrite structure, this becomes $(Mn_xFe_{1-x})_3O_{4.3}$, where x ranges from 0.42 to 0.47 for
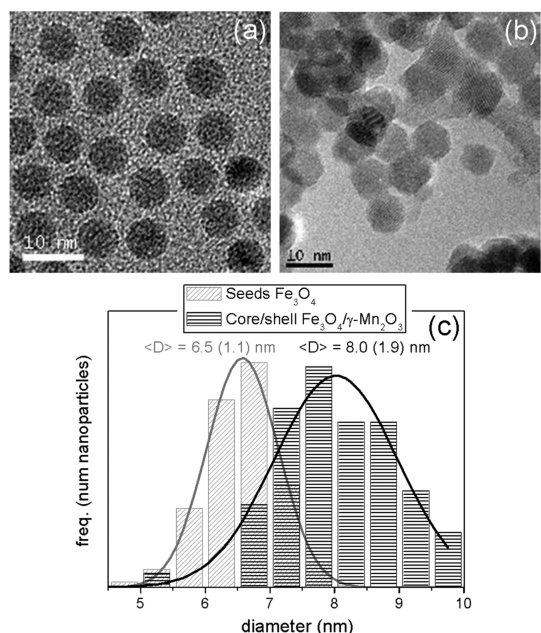
Figure 6. TEM image of (a) Fe_3O_4 seeds and (b) $Fe_3O_4|$ γ-Mn_2O_3 core|shell nanoparticles. (c) Particle size distribution comparing the particles in (a) and (b). The lines show the fit of the experimental data to a log-normal distribution. The values given in the figure correspond to the mean value and the log-normal standard deviation.

inner and outer shell regions, respectively. This is surprisingly close to the previously extracted *x* of 0.40 to 0.46 using Fe_3O_4 and γ-Mn_2O_3 as inputs. Our conclusion is that the extracted scattering profile shapes and corresponding chemical compositions are largely independent of oxide inputs used.

Size Distribution *via* TEM. The overall diameter of the core|shell nanoparticles obtained from TEM (Figure 6a–c) of 8.0 ± 1.9 nm corresponds satisfactorily with ASAXS analysis at 8.2 ± 0.2 nm. On the other hand, the size of the core|shell Fe_3O_4 cores obtained from ASAXS (≈0.8 nm) is remarkably small since the original Fe_3O_4 seeds used are 6.5 ± 1.1 nm (see Figure 6a,c). The reduction in diameter of the pure Fe_3O_4 core regions within the core|shell particles from that of the uncoated Fe_3O_4 seeds indicates that some of the Fe_3O_4 reacts with the γ-Mn_2O_3 and is incorporated in a mixed-metal outer shell, as has been observed for similar particles.[27,36] In fact, the degree of interdiffusion between Mn and Fe and the exact Mn oxide phase in this type of nanoparticles depends critically on the temperature at which the nanoparticles are exposed to air and on the size of the nanoparticles.[27,36,42,43] The presence of uncoated Fe_3O_4 seeds evidenced by the bimodal distribution of Fe_3O_4 nanoparticles in the ASAXS analysis is not obvious from the TEM analysis. However, it may explain the unusually large increase in log-normal standard deviation in the core|shell nanoparticles with respect to the original seeds (see Figure 6c). In fact, closer inspection of the particle size distribution of the core|shell nanoparticles reveals an asymmetric tail of the distribution toward smaller sizes.
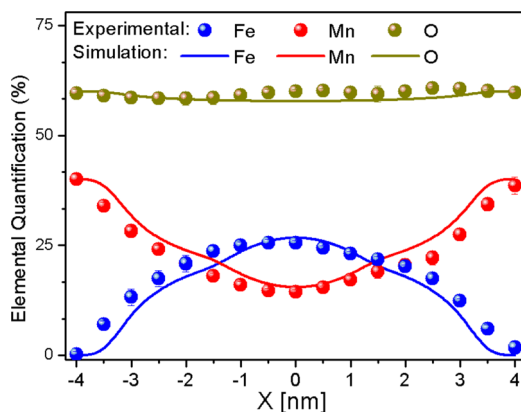

Figure 7. Averaged Fe, Mn, and O elemental quantification from nanoparticles shown in Figure 1 and a simulation considering a 2.5 nm (radius) Fe_3O_4 core|1 nm $MnFe_2O_4$|0.5 nm γ-Mn_2O_3.

This part of the distribution might be associated with the uncoated Fe_3O_4 nanoparticles, which according to ASAXS, are much smaller (≈2.2 to 3.4 nm) than the mean size of the seeds (6.5 nm). Accordingly, Ostwald ripening is likely the mechanism by which the relatively larger core|shell nanoparticles grow at the expense of the smaller ones, thereby redissolving the manganese oxide shell from the small seeds,[44] although traces of Mn on the uncoated seeds cannot be ruled out.

Core|Shell Evidence *via* EELS. The imaging of the local composition of the core|shell nanoparticles using STEM EELS mapping clearly reveals a multilayered structure with an Fe-based core and a Mn-rich shell (Figure 1). Quantitatively, EELS yields a 2.5 nm (core radius) Fe_3O_4|1 nm (inner shell) $MnFe_2O_4$|0.5 nm (outer shell) γ-Mn_2O_3 (Figure 7). This is in qualitative agreement with the ASAXS core|graded shell structure, where both approaches clearly show the presence of an intermixed shell structure and a reduced core size (with respect to the seeds). Nevertheless, the ASAXS analysis indicates a more delocalized distribution of the Fe compared with the EELS results. However, it is important to emphasize that the EELS results are based on a handful of nanoparticles, while ASAXS measures the ensemble-average. Importantly, EEL spectra at different magnifications (see Figure S1 in the Supporting Information) demonstrate that the Mn|Fe intensity ratio remains constant, indicating that the overall composition of the sample is approximately the same independent of the number of particles investigated.

Structural Characterization. High-resolution scanning transmission electron microscopy (HR-STEM) and its corresponding fast Fourier transform (FFT) (Figure 8a, b) indicate that two distinctive spinel crystalline phases coexist within the same nanoparticle, one cubic and one tetragonal. Longer-ranged X-ray diffraction (XRD) (Figure 8c) confirms the existence of cubic and tetragonal spinel phases. Given that Fe-rich regions in the Fe–Mn oxide phase diagram ($MnFe_2O_4$–Fe_3O_4) form a
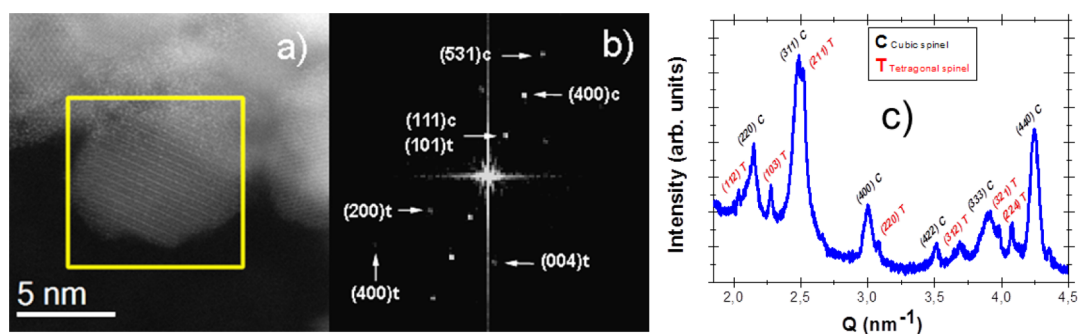
Figure 8. (a) HR-STEM image for the core|shell nanoparticle and (b) FFT of the highlighted in (a). (c) X-ray diffraction. Cubic and tetragonal spinel structures are labeled as c and t, respectively.

cubic spinel, while Mn-rich regions ($FeMn_2O_4$–Mn_3O_4) form a tetragonal spinel,[45] we identify the cubic structure as arising from the core and the tetragonal one from the shell. In fact, the ratio of intensities between the tetragonal and cubic phases from XRD is in concordance with a core|shell structure with a cubic spinel core and a thin tetragonal spinel shell.

Spectroscopic Techniques. Apart from two weak resonances (α and δ),[46−49] electron spin resonance (ESR) produces distinctive resonances, β and ξ, as a function of temperature (see details in the Supporting Information, Figure S2). The more intense β line broadens and shifts toward a lower field[50] as the temperature decreases (Figure S3) and is qualitatively similar to the spectra reported for Fe_3O_4 nanoparticle systems,[51−53] while the ξ line width remains almost unchanged down to 50 K and broadens[54] below this (Figure S3), consistent with either Mn_3O_4[42,55−57] or a $Mn_xFe_{3−x}O_4$ spinel.[58]

On the basis of previous studies on Fe, Mn, and FeMn oxides,[59−64] XAS and X-ray magnetic circular dichroism (XMCD) indicate that the Fe exists in a near single phase, whereas the Mn clearly exists in mixed oxidation states corresponding to multiple crystalline phases (see detailed description in the Supporting Information, Figure S4). Thus, the complementary spectroscopic measurements indicate the presence of multiple phases, consistent with the ASAXS modeling results of a $(Mn_xFe_{1−x})_3O_4$ core|shell|shell morphology with increasing Mn content toward the surface.

CONCLUSIONS

In summary, we have demonstrated that multiple-energy ASAXS provides significant enhancement in sensitivity to internal material boundaries of layered nanoparticles compared with the traditional modeling of a single scattering energy, even for cases in which high scattering length density (ρ) contrast between the constituent materials exists. Applied to a system of nominal core|shell Fe_3O_4|γ-Mn_2O_3 nanoparticles, this technique revealed that the core|shell nanoparticles comprise a graded nanoparticle tending toward Fe_3O_4 at the center, yet retaining a significant portion of Fe out to the exterior. The average Fe−Mn oxide shell composition can be recast in terms of a ferrite structure as $(Mn_xFe_{1−x})_3O_{\approx4}$ with x ranging from 0.40 (interior shell of diameter 0.8 to 4.8 nm) to 0.46 (exterior shell of diameter 4.8 to 8.2 nm). The presence of a small fraction of uncoated Fe_3O_4 seeds explains the smearing of the Fe_3O_4 scattering contribution without assigning undue polydispersity. The model-derived concept of a dual distribution of core|shell nanoparticles plus uncoated seeds is further corroborated by both a shift in low-Q peak placement at the Fe K-edge and a measurable difference between structure factors $S_{Fe_3O_4}$ and $S_{\gamma-Mn_2O_3}$ obtained from analysis of the derived interference term, $\mathcal{F}_{Int1}$. These fine details revealed through the direct contrast of the material-specific scattering profiles simply could not have been obtained from simultaneous fitting of the resonant data as is generally practiced. The results, although they are in concordance with TEM, EELS, HR-STEM, XRD, ESR, XAS, and XMCD analysis, evidence ensemble-averaged structural details which would have been difficult to access using solely these studies. Given how dependent core|shell nanoparticle behavior and functionality often are on internal structure, multiple-energy ASAXS shows great promise in the rapidly developing field of nanoparticle research.

METHODS

Synthesis. The synthesis of core|shell particles was carried out following a multistep procedure where preformed iron oxide nanoparticles were used as seeds for the subsequent growth of manganese(II) oxide and its passivation to form γ-Mn_2O_3.[36] Briefly, an iron(III) oleate precursor was prepared following a similar procedure reported earlier.[65] First, 14 mmol of iron(III) chloride ($FeCl_3\cdot6H_2O$, 97%, Aldrich) and 42 mmol of

sodium oleate (NaOl, Riedel-de Haën) were dissolved in 21 mL of ethanol (99.5%, Panreac), 28 mL of deionized water, and 50 mL of hexane (Fluka) and refluxed under magnetic stirring for 3 h. During this time, it is possible to see that the precursor changes from a light red color to a burgundy red, indicating the formation of the precursor. The organic phase was washed with 5 mL of deionized water three times and dried under vacuum. In a typical synthesis, spheroidal particles with a particle diameter

$D = 6.5 \pm 1.1$ nm were prepared by dissolving 3 mmol of the precursor and 3 mmol of oleic acid (OlOH, Aldrich) in 36 mL of 1-octadecene (ODE 90%, Aldrich) at 70 °C. The mixture was heated to 320 °C (at 5 °C/min) under stirring at 130 rpm and kept for 30 min. The reaction vessel was allowed to cool to room temperature before exposure to air. The particles were retrieved by several cycles of centrifugation at 2000g, disposal of supernatant, redispersion in hexane, and coagulation with ethanol.

The manganese oxide layers were laid on the iron-oxide-based nanoparticles, modifying an earlier reported procedure used for the synthesis of MnO|γ-Mn$_2$O$_3$ nanoparticles.[42,66] The procedure is as follows: 30 mg of iron oxide seeds, 2.3 mmol of 1,2-hexadecanediol (HDD, Aldrich), and 1.9 mmol of manganese(II) acetylacetonate (Mn(acac)$_2$, Aldrich) were added to 150 mL of benzylether (Bz$_2$O, Fluka) together with 5 mL (16 mmol) of oleic acid (OlOH, Aldrich) and 50 mL of oleylamine (OlNH$_2$, Fluka). The slurry was deaerated with Ar for 15 min. The slurry was then heated at $\sim$7 °C/min to 200 °C, allowed to proceed under reflux with a residence time, $t \sim 60$ min, and then removed from the heating source and allowed to cool to room temperature. The particles were washed from the reaction media by subsequent steps of precipitation under ethanol, centrifugation, and redispersion in hexane.

Small-Angle Neutron Scattering (SANS). SANS patterns were collected at room temperature at the NIST Center for Neutron Research beamline NG3. The incident wavelength was 0.5 nm with 11% wavelength spread.

Anomalous Small-Angle X-ray Scattering (ASAXS). SAXS patterns were measured at room temperature at the Mn and Fe K-edges (6535 and 7112 eV, respectively)[41] and off-resonance (6000 eV) at the Advanced Photon Source beamline 6-ID-B. The scattering data were collected using a SII Nano Technology Vortex detector.[67] This type of detector was selected because it has an energy discrimination of 134 eV, which was used to separate the desired elastic X-ray scattering from the background fluorescence (which can be non-negligible near absorption edges).

The incident beam intensity was monitored using a high-voltage ion chamber. The detector/monitor response was calibrated as a function of incident X-ray energy by measuring the fluorescence produced by a vanadium thin film (with its own well-known energy response curve[41]) over the range of 6.0 to 9.0 keV. The detector/monitor response was fit and well described by a linear function over this energy range. The absorption of the nanoparticles as a function of energy was measured *via* transmission through the nanoparticle sample at 6000, 6535, and 7112 eV. Finally, the elastic, small-angle scattering patterns obtained at the same set of incident X-ray energies were measured with the SII Nano Technology Vortex detector[67] and were normalized by (i) the ion chamber (measure of incident intensity), (ii) the detector/monitor energy response, and (iii) the sample transmission values at the corresponding energies, respectively.

Transmission Electron Microscopy (TEM) and Electron Energy Loss Spectroscopy (EELS). TEM images were obtained using a JEM-2100[67] with a LaB$_6$ filament and a JEM-2010F[67] with a field-emission gun operating at 200 kV, the latter equipped with a postcolumn Gatan image filter (GIF) energy spectrometer. Global EEL spectra were taken at different TEM magnifications at an energy range containing the O K-, Mn L$_{2,3}$-, and Fe L$_{2,3}$-edges. Moreover, local EEL spectra were acquired at different positions along the diameter of the nanoparticles on the L-edge of Mn and Fe with an energy resolution of 0.8 eV. The quantitative analysis of the EELS spectra was performed using the homemade software package MANGANITAS.[67−69]

High-Resolution Scanning Tunneling Electron Microscopy (HR-STEM) and EELS Mapping. HR-STEM and EELS have been obtained in a FEI Titan low-base[67] operating at 300 kV (HR-STEM). The indexing of the FFT of HR-STEM image (Figure 8) reveals the presence of two different crystallographic phases, related to iron oxide cubic spinel phase (JCPDS Card No. 82-1533) in the core and manganese oxide tetragonal spinel (JCPDS Card No. 24-0734) in the shell.

X-ray Diffraction (XRD). XRD patterns were collected using a Panalytical X'Pert Pro diffractometer[67] with Cu Kα radiation.

Electron Spin Resonance (ESR). ESR measurements were performed in an ESP-300 Bruker spectrometer,[67] operating at a frequency $\nu \sim 9.5$ GHz (X-band), and in the $3-300$ K temperature

range. In order to avoid spurious signals, care was taken to not saturate the cavity due to the giant ESR sample signal. For this purpose, and to ensure good penetration of the microwaves into the sample, the Fe$_3$O$_4$|γ-Mn$_2$O$_3$ nanoparticles were diluted in a nonabsorbing KCl salt. No noticeable changes of the cavity coupling were registered in the whole set of experiments. From the ESR spectra, we derived the resonance field H_r, the peak-to-peak line width ΔH, and the ESR intensity. From the resonance condition, $h\nu = g\mu_B H_r$ (where h and μ_B are the Plank constant and the Bohr magneton, respectively), the gyromagnetic g-factor was obtained, and the spectrum intensity is the area under the absorption curve. As the materials studied in this work are powder samples, the observed spectra present inhomogeneous broadening due to the angular, size, and shape distribution.

X-ray Absorption Spectroscopy (XAS) and X-ray Magnetic Circular Dichroism (XMCD). XAS and XMCD measurements were performed on dried core|shell nanoparticles spread onto carbon tape at the SIM beamline of the Swiss Light Source (SLS) of the Paul Scherrer Institute. Both XAS and XMCD spectra were recorded at the Fe and Mn L$_{3,2}$-edges using total electron yield (TEY) mode at 10 K in a magnetic field of 5 T after field cooling (FC) from 300 K under an applied field of 5 T. The XMCD signal was normalized by the area of the XAS spectra after correcting for the background.

Conflict of Interest: The authors declare no competing financial interest.

Supporting Information Available: Additional experimental details and figures. This material is available free of charge *via* the Internet at http://pubs.acs.org.

REFERENCES AND NOTES

1. Kallinteri, P.; Higgins, S.; Hutcheon, G. A.; St. Pourçain, C. B.; Garnett, M. C. Novel Functionalized Biodegradable Polymers for Nanoparticle Drug Delivery Systems. *Biomacromolecules* **2005**, *6*, 1885–1894.

2. Davis, M. E.; Chen, Z.; Shin, D. M. Nanoparticle Therapeutics: An Emerging Treatment Modality for Cancer. *Nat. Rev. Drug Discovery* **2008**, *7*, 771–782.

3. Frey, N. A.; Peng, S.; Cheng, K.; Sun, S. Magnetic Nanoparticles: Synthesis, Functionalization, and Applications in Bioimaging and Magnetic Energy Storage. *Chem. Soc. Rev.* **2009**, *38*, 2532–2542.

4. Sharma, R.; Chen, C. Newer Nanoparticles in Hyperthermia Treatment and Thermometry. *J. Nanopart. Res.* **2009**, *11*, 671–689.

5. Mishra, B.; Patel, B. B.; Tiwari, S. Colloidal Nanocarriers: A Review on Formulation Technology, Types and Applications toward Targeted Drug Delivery. *Nanomed. Nanotechnol. Biol. Med.* **2010**, *6*, 9–24.

6. Costi, R.; Saunders, A.; Banin, U. Colloidal Hybrid Nano-structures: A New Type of Functional Materials. *Angew. Chem., Int. Ed.* **2010**, *49*, 4878–4897.

7. Carbone, L.; Cozzoli, P. D. Colloidal Heterostructured Nanocrystals: Synthesis and Growth Mechanisms. *Nano Today* **2010**, *5*, 449–493.

8. Schärtl, W. Current Directions in Core−Shell Nanoparticle Design. *Nanoscale* **2010**, *2*, 829–843.

9. Ijiri, Y.; Kelly, C. V.; Borchers, J. A.; Rhyne, J. J.; Farrell, D. F.; Majetich, S. A. Detection of Spin Coupling in Iron Nano-particles with Small Angle Neutron Scattering. *Appl. Phys. Lett.* **2005**, *86*, 243102.

10. Kechrakos, D.; Trohidou, K.; Vasilakaki, M. Magnetic Properties of Dense Nanoparticle Arrays with Core/Shell Morphology. *J. Magn. Magn. Mater.* **2007**, *316*, e291–e294.

11. Golosovsky, I. V.; Salazar-Alvarez, G.; López-Ortega, A.; González, M. A.; Sort, J.; Estrader, M.; Suriñach, S.; Baró, M. D.; Nogués, J. Magnetic Proximity Effect Features in Antiferromagnetic/Ferrimagnetic Core−Shell Nanoparticles. *Phys. Rev. Lett.* **2009**, *102*, 247201.

12. Inderhees, S. E.; Borchers, J. A.; Green, K. S.; Kim, M. S.; Sun, K.; Strycker, G. L.; Aronson, M. C. Manipulating the Magnetic Structure of Co Core/CoO Shell Nanoparticles: Implications for Controlling the Exchange Bias. *Phys. Rev. Lett.* **2008**, *101*, 117202.

13. Berkowitz, A. E.; Rodriguez, G. F.; Hong, J. I.; An, K.; Hyeon, T.; Agarwal, N.; Smith, D. J.; Fullerton, E. E. Antiferromagnetic MnO Nanoparticles with Ferrimagnetic Mn_3O_4 Shells: Doubly Inverted Core−Shell System. *Phys. Rev. B* **2008**, *77*, 024403.

14. Elder, S. H.; Cot, F. M.; Su, Y.; Heald, S. M.; Tyryshkin, A. M.; Bowman, M. K.; Gao, Y.; Joly, A. G.; Balmer, M. L.; Kolwaite, A. C.; *et al.* The Discovery and Study of Nanocrystalline TiO_2-(MoO_3) Core−Shell Materials. *J. Am. Chem. Soc.* **2000**, *122*, 5138–5146.

15. Peng, S.; Lei, C.; Ren, Y.; Cook, R. E.; Sun, Y. Plasmonic/Magnetic Bifunctional Nanoparticles. *Angew. Chem., Int. Ed.* **2011**, *50*, 3158–3163.

16. Song, J.-H.; Atay, T.; Shi, S.; Urabe, H.; Nurmikko, A. V. Large Enhancement of Fluorescence Efficiency from CdSe/ZnS Quantum Dots Induced by Resonant Coupling to Spatially Controlled Surface Plasmons. *Nano Lett.* **2005**, *5*, 1557–1561.

17. Joo, S. H.; Park, J. Y.; Tsung, C.-K.; Yamada, Y.; Yang, P.; Somorjai, G. A. Thermally Stable Pt/Mesoporous Silica Core−Shell Nanocatalysts for High-Temperature Reactions. *Nat. Mater.* **2009**, *8*, 126–131.

18. Bruchez, M., Jr.; Moronne, M.; Gin, P.; Weiss, S.; Alivisatos, A. P. Semiconductor Nanocrystals as Fluorescent Biological Labels. *Science* **1998**, *281*, 2013–2016.

19. Brodbeck, C. M.; Bukrey, R. R. Model Calculations for the Coordination of Fe^{3+} and Mn^{2+} Ions in Oxide Glasses. *Phys. Rev. B* **1981**, *24*, 2334–2343.

20. Trudel, S.; Jones, C. H. W.; Hill, R. H. Magnetic Properties of Nanocrystalline Iron Oxide/Amorphous Manganese Oxide Nanocomposite Thin Films Prepared *via* Photochemical Metal-Organic Deposition. *J. Mater. Chem.* **2007**, *17*, 2206.

21. Rojas, T. C.; Sayagues, M. J.; Caballero, A.; Koltypin, Y.; Gedanken, A.; Ponsonnet, L.; Vacher, B.; Martin, J. M.; Fernandez, A. TEM, EELS and EFTEM Characterization of Nickel Nanoparticles Encapsulated in Carbon. *J. Mater. Chem.* **2000**, *10*, 715–721.

22. Cho, S.-J.; Idrobo, J.-C.; Olamit, J.; Liu, K.; Browning, N. D.; Kauzlarich, S. M. Growth Mechanisms and Oxidation Resistance of Gold-Coated Iron Nanoparticles. *Chem. Mater.* **2005**, *17*, 3181–3186.

23. Teng, X.; Yang, H. Synthesis of Magnetic Nanocomposites and Alloys from Platinum-Iron Oxide Core−Shell Nano-particles. *Nanotechnology* **2005**, *16*, S554–S561.

24. Bao, Y.; Calderon, H.; Krishnan, K. M. Synthesis and Char-acterization of Magnetic-Optical Core−Shell Nanoparticles. *J. Phys. Chem. C* **2007**, *111*, 1941–1944.

25. Wang, J. X.; Inada, H.; Wu, L.; Zhu, Y.; Choi, Y.; Liu, P.; Zhou, W.-P.; Adzic, R. R. Oxygen Reduction on Well-Defined Core−Shell Nanocatalysts: Particle Size, Facet, and Pt Shell

26. Koh, A. L.; Bao, K.; Khan, I.; Smith, W. E.; Kothleitner, G.; Nordlander, P.; Maier, S. A.; McComb, D. W. Electron Energy-Loss Spectroscopy (EELS) of Surface Plasmons in Single Silver Nanoparticles and Dimers: Influence of Beam Damage and Mapping of Dark Modes. *ACS Nano* **2009**, *3*, 3015–3022.

27. Estradé, S.; Yedra, L.; López-Ortega, A.; Estrader, M.; Salazar-Alvarez, G.; Baró, M.; Nogués, J.; Peiró, F. Distinguishing the Core from the Shell in MnO_x/MnO_y and FeO_x/MnO_x Core/Shell Nanoparticles through Quantitative Electron Energy Loss Spectroscopy (EELS) Analysis. *Micron* **2012**, *43*, 30–36.

28. Rieker, T.; Hanprasopwattana, A.; Datye, A.; Hubbard, P. Particle Size Distribution Inferred from Small-Angle X-ray Scattering and Transmission Electron Microscopy. *Langmuir* **1999**, *15*, 638–641.

29. Vonk, C. G. On Two Methods of Determination of Particle Size Distribution Functions by Means of Small-Angle X-ray Scattering. *J. Appl. Crystallogr.* **1976**, *9*, 433–440.

30. Karle, J. The Relative Scaling of Multiple-Wavelength Anomalous Dispersion Data. *Acta Crystallogr., Sect. A* **1984**, *40*, 1–4.

31. Hendrickson, W. A. Determination of Macromolecular Structures from Anomalous Diffraction of Synchrotron Radiation. *Science* **1991**, *254*, 51–58.

32. Stauber, D. J.; DiGabriele, A. D.; Hendrickson, W. A. Structural Interactions of Fibroblast Growth Factor Recep-tor with Its Ligands. *Proc. Natl. Acad. Sci. U.S.A.* **2000**, *97*, 49–54.

33. Miao, J.; Charalambous, P.; Kirz, J.; Sayre, D. Extending the Methodology of X-ray Crystallography To Allow Imaging of Micrometre-Sized Non-crystalline Specimens. *Nature* **1999**, *400*, 342–344.

34. Barnardo, T.; Hoydalsvik, K.; Winter, R.; Martin, C. M.; Clark, G. F. *In Situ* Double Anomalous Small-Angle X-ray Scattering of the Sintering and Calcination of Sol−Gel Prepared Yttria-Stabilized-Zirconia Ceramics. *J. Phys. Chem. C* **2009**, *113*, 10021–10028.

35. Haug, J.; Kruth, H.; Dubiel, M.; Hofmeister, H.; Haas, S.; Tatchev, D.; Hoell, A. ASAXS Study on the Formation of Core−Shell Ag/Au Nanoparticles in Glass. *Nanotechnology* **2009**, *20*, 505705.

36. Salazar-Alvarez, G.; Lidbaum, H.; López-Ortega, A.; Estrader, M.; Leifer, K.; Sort, J.; Suriñach, S.; Baró, M. D.; Nogués, J. Two-, Three-, and Four-Component Magnetic Multilayer Onion Nanoparticles Based on Iron Oxides and Manganese Oxides. *J. Am. Chem. Soc.* **2011**, *133*, 16738–16741.

37. Kline, S. R. Reduction and Analysis of SANS and USANS Data Using IGOR Pro. *J. Appl. Crystallogr.* **2006**, *39*, 895–900.

38. DeTitta, G. T.; Weeks, C. M.; Thuman, P.; Miller, R.; Hauptman, H. A. Structure Solution by Minimal-Function Phase Refinement and Fourier Filtering. I. Theoretical Basis. *Acta Crystallogr., Sect. A* **1994**, *50*, 203–210.

39. Weeks, C. M.; DeTitta, G. T.; Hauptman, H. A.; Thuman, P.; Miller, R. Structure Solution by Minimal-Function Phase Refinement and Fourier Filtering. II. Implementation and Applications. *Acta Crystallogr., Sect. A* **1994**, *50*, 210–220.

40. Materlik, G., Sparks, C. J., Fischer, K., Eds. *Resonant Anomalous X-Ray Scattering: Theory and Applications*; Elsevier: North-Holland, The Netherlands, 1994.

41. Henke, B.; Gullikson, E.; Davis, J. X-ray Interactions: Photo-absorption, Scattering, Transmission, and Reflection at $E = 50-30,000$ eV, $Z = 1-92$. *At. Data Nucl. Data Tables* **1993**, *54*, 181–342.

42. López-Ortega, A.; Tobia, D.; Winkler, E.; Golosovsky, I. V.; Salazar-Alvarez, G.; Estradé, S.; Estrader, M.; Sort, J.; González, M. A.; Suriñach, S.; *et al.* Size-Dependent Passivation Shell and Magnetic Properties in Antiferromagnetic/Ferrimagnetic Core/Shell MnO Nanoparticles. *J. Am. Chem. Soc.* **2010**, *132*, 9398–9407.

43. López-Ortega, A.; Estrader, M.; Salazar-Alvarez, G.; Golosovsky, I. V.; Dumas, R. K.; Keavney, D. J.; Vasilakaki, M.; Trohidou, K. N.;

Sort, J.; Peiró, F.; *et al.* Strongly Exchange Coupled Inverse Ferrimagnetic Soft/Hard, $Mn_xFe_{3-x}O_4/Fe_xMn_{3-x}O_4$, Core/Shell Heterostructured Nanoparticles. *Nanoscale* **2012**, *4*, 5138–5147.

44. Li, Q.; Wang, J.; He, Y.; Liu, W.; Qiu, X. Growth of Nearly Monodisperse MnO Nanocrystals in a Two-Size Distribution System. *Cryst. Growth Des.* **2009**, *9*, 3100–3103.

45. Guillemet-Fritsch, S.; Navrotsky, A.; Tailhades, P.; Coradin, H.; Wang, M. J. Thermochemistry of Iron Manganese Oxide Spinels. *J. Solid State Chem.* **2005**, *178*, 106–113.

46. Castner, T.; Newell, G. S.; Holton, W. C.; Slichter, C. P. Note on the Paramagnetic Resonance of Iron in Glass. *J. Chem. Phys.* **1960**, *32*, 668–673.

47. Winkler, E.; Fainstein, A.; Etchegoin, P.; Fainstein, C. Fe Impurities in L-Alanine: An EPR, Luminescence, and Raman Study. *Phys. Rev. B* **1999**, *59*, 1255–1262.

48. Winkler, E.; Zysler, R. D.; Fiorani, D. Surface and Magnetic Interaction Effects in Mn_3O_4 Nanoparticles. *Phys. Rev. B* **2004**, *70*, 174406.

49. Abragam, A., Bleaney, B., Eds. *Electron Paramagnetic Resonance of Transition Ions*; Dover Publications: New York, 1986.

50. Fainstein, A.; Winkler, E.; Butera, A.; Tallon, J. Magnetic Interactions and Magnon Gap in the Ferromagnetic Superconductor $RuSr_2GdCu_2O_8$. *Phys. Rev. B* **1999**, *60*, 12597–12600.

51. Pal, S.; Dutta, P.; Shah, N.; Huffman, G. P.; Seehra, M. S. Surface Spin Disorder in Fe_3O_4 Nanoparticles Probed by Electron Magnetic Resonance Spectroscopy and Magnetometry. *IEEE Trans. Magn.* **2007**, *43*, 3091–3093.

52. Koseoglu, Y. Effect of Surfactant Coating on Magnetic Properties of Fe_3O_4 Nanoparticles: An FMR Study. *J. Magn. Magn. Mater.* **2006**, *300*, e327–e330.

53. Hsu, K. H.; Wu, J. H.; Huang, Y. Y.; Wang, L. Y.; Lee, H. Y.; Lin, J. G. Critical Size Effects on the Magnetic Resonance in Fe_3O_4 Nanoparticles. *J. Appl. Phys.* **2005**, *97*, 114322.

54. de Biasi, E.; Ramos, C.; Zysler, R. Size and Anisotropy Determination by Ferromagnetic Resonance in Dispersed Magnetic Nanoparticle Systems. *J. Magn. Magn. Mater.* **2003**, *262*, 235–241.

55. Chen, Z.; Zhang, S.; Tan, S.; Li, F.; Wang, J.; Jin, S.; Zhang, Y. Preparation and Electron Spin Resonance Effect of Nanometer-Sized Mn_2O_3. *J. Cryst. Growth* **1997**, *180*, 280–283.

56. Seehra, M. S.; Srinivasan, G. Electron Spin Resonance of Mn_3O_4 Defects in MnO. *J. Appl. Phys.* **1982**, *53*, 8345–8347.

57. Srinivasan, G.; Seehra, M. S. Magnetic Properties of Mn_3O_4 and a Solution of the Canted-Spin Problem. *Phys. Rev. B* **1983**, *28*, 1–7.

58. Kliava, J.; Edelman, I.; Ivanova, O.; Ivantsov, R.; Petrakovskaja, E.; Hennet, L.; Thiaudière, D.; Saboungi, M. Electron Magnetic Resonance and Magnetooptical Studies of Nanoparticle-Containing Borate Glasses. *J. Magn. Magn. Mater.* **2011**, *323*, 451–460.

59. Abbate, M.; Goedkoop, J. B.; Groot, M. F. D.; Grioni, M.; Fuggle, J. C.; Hofmann, S.; Petersen, H.; Sacchi, M. Probing Depth of Soft-X-ray Absorption Spectroscopy in Total Electron Yield Mode. *Surf. Interface Anal.* **1992**, *18*, 65–69.

60. Lee, H. J.; Kim, G.; Kim, D. H.; Kang, J.-S.; Zhang, C. L.; Cheong, S. W.; Shim, J. H.; Lee, S.; Lee, H.; Kim, J.-Y.; *et al.* Valence States and Occupation Sites in (Fe, Mn)$_3O_4$ Spinel Oxides Investigated by Soft X-ray Absorption Spectroscopy and Magnetic Circular Dichroism. *J. Phys.: Condens. Matter* **2008**, *620*, 295203.

61. Bayer, V.; Podloucky, R.; Franchini, C.; Allegretti, F.; Xu, B.; Parteder, G.; Ramsey, M. G.; Surnev, S.; Netzer, F. P. Formation of $Mn_3O_4(001)$ on MnO(001): Surface and Interface Structural Stability. *Phys. Rev. B* **2007**, *76*, 165428.

62. Chen, C. L. Electronic and Magnetic Properties of Transition Metal Ferrites and Superlattice Studied by X-ray Absorption Spectroscopy; Ph.D. Thesis, Tamkang University, 2005.

63. Pellegrin, E.; Hagelstein, M.; Doyle, S.; Moser, H. O.; Fuchs, J.; Vollath, D.; Schuppler, S.; James, M. A.; Saxena, S. S.; Niesen, L.; *et al.* Characterization of Nanocrystalline γ-Fe_2O_3 with

64. Pool, V.; Klem, M.; Jolley, C.; Arenholz, E. A.; Douglas, T.; Young, M.; Idzerda, Y. U. Site Determination and Magnetism of Mn Doping in Protein Encapsulated Iron Oxide Nanoparticles. *J. Appl. Phys.* **2010**, *107*, 09B517.

65. Park, J.; An, K.; Hwang, Y.; Park, J.-G.; Noh, H.-J.; Kim, J.-Y.; Park, J.-H.; Hwang, N.-M.; Hyeon, T. Ultra-Large-Scale Syntheses of Monodisperse Nanocrystals. *Nat. Mater.* **2004**, *3*, 891–895.

66. Salazar-Alvarez, G.; Sort, J.; Suriñach, S.; Baró, M. D.; Nogués, J. Synthesis and Size-Dependent Exchange Bias in Inverted Core–Shell MnO|Mn_3O_4 Nanoparticles. *J. Am. Chem. Soc.* **2007**, *129*, 9102–9108.

67. Certain commercial equipment, instruments, and software, have been identified in this paper to foster understanding. Such identification does not imply recommendation or endorsement by the National Institute of Standards and Technology, nor does it imply that the materials or equipment identified are necessarily the best available for the purpose.

68. Estradé, S.; Arbiol, J.; Peiró, F.; Abad, L.; Laukhin, V.; Balcells, L.; Martínez, B. Cationic Diffusion in $La_{2/3}Ca_{1/3}MnO_3$ Thin Films Grown on $LaAlO_3$ (001) Substrates. *Appl. Phys. Lett.* **2007**, *91*, 252503.

69. Estradé, S.; Arbiol, J.; Peiró, F.; Infante, I. C.; Sanchéz, F.; Fontcuberta, J.; de la Peña, F.; Walls, M.; Colliex, C. Cationic and Charge Segregation in $La_{2/3}Ca_{1/3}MnO_3$ Thin Films Grown on (001) and (110) $SrTiO_3$. *Appl. Phys. Lett.* **2008**, *93*, 112505.

Synchrotron Radiation Techniques. *Phys. Status Solidi B* **1999**, *215*, 797–801.